Journal of Materials Science & Technology 35 (2019) 1354–1363

Contents lists available at ScienceDirect

Journal of Materials Science & Technology

journal homepage: www.jmst.org

Research Article

Grain size-dependent Mg/Si ratio effect on the microstructure and mechanical/electrical properties of Al-Mg-Si-Sc alloys

Shengyu Jiang, Ruihong Wang*

School of Materials Science and Engineering, Xi'an University of Technology, Xi'an, 710048, China

ARTICLE INFO

Article history:
Received 31 August 2018
Received in revised form 2 October 2018
Accepted 5 October 2018
Available online 8 March 2019

Keywords:
Al-Mg-Si-Sc
Grain size effect
Mg/Si ratio
Precipitation
Hardness/conductivity

ABSTRACT

Al-Mg-Si-Sc alloys with different Mg/Si ratio (<1.73 in wt.% *vs*>1.73 in wt.%) and different grain size (coarse grains *vs* ultrafine grains) were prepared, which allowed to investigate the grain size-dependent Mg/Si ratio effect on the microstructural evolution and concomitantly on the hardness and electrical conductivity when subjected to aging at 200 °C. In the coarse-grained Al-Mg-Sc-Sc alloys, the β'' precipitation within the grain interior and also the precipitation hardening were highly dependent on the Mg/Si ratio, while the electrical conductivity was slightly affected by the Mg/Si ratio. A promoted β'' precipitation was found in the case of Si excess (Mg/Si ratio <1.73), much greater than in the case of Mg excess (Mg/Si ratio>1.73). While in the ultrafine-grained Al-Mg-Si-Sc alloys, the electrical conductivity rather than the hardness was more sensitive to the Mg/Si ratio. The alloy with Si excess displayed electrical conductivity much higher than its counterpart with Mg excess. This is rationalized by the grain boundary precipitation promoted by Si, which reduced the solute atoms and precipitates within the grain interior. Age softening was found in the ultrafine-grained alloy with Si excess, but the ultrafine-grained alloy with Mg excess held the hardness almost unchanged during the aging. The hardness-conductivity correlation is comprehensively discussed by considering the coupling effect of Mg/Si ratio and grain size. A strategy to simultaneously increase the hardness/strength and electrical conductivity is proposed for the Al-Mg-Si-Sc alloys, based on present understanding of the predominant factors on strengthening and conductivity, respectively.

1. Introduction

The age-treatable Al-Mg-Si alloys, known as 6xxx series Al alloys, have been widely used as structural materials in automotive and aviation industries [1,2]. Due to their low density, high specific strength, and relatively high electrical conductivity, the Al-Mg-Si alloys are also considered as the candidates for application in electrical fields [3,4]. A typical decomposition sequence of supersaturated solid solution (SSS) of the Al-Mg-Si alloys proceeds in following order: SSS → early precipitation stages (GP zones) → β'' phase → β' phase→ β phase (Mg_2Si) [5,6]. Both the strength and the electrical conductivity are highly dependent on the precipitation behaviors. However, the two properties are mutually exclusive: a higher strength is usually accompanied with a lower electrical conductivity, and *vice versa*. The set balance of strength and electrical conductivity is generally tuned through thermal and thermomechanical treatments, where the key is to manipulate the precipitation [7,8].

In the Al-Mg-Si alloys where Mg and Si are the main alloying elements, it is claimed [9–12] that the Mg/Si ratio impacts on the precipitations remarkably. Since the Mg/Si mass ratio in Mg_2Si is about 1.73, the added Mg and Si elements will be all consumed to form Mg_2Si particles ideally, provided the nominal Mg/Si ratio is equal to 1.73. Excess Mg or excess Si in addition may have some effects on the precipitation and concomitantly on the mechanical properties /electrical conductivity. Available studies showed that increasing the Si content usually resulted in more formable alloys with higher strengths, for which the main reason is that excess Si promoted the uniform precipitation of fine β'' precipitates [9]. Excess Si also decreased the lattice distortion, contributing to the enhancement of conductivity [9]. On the contrary, excess Mg led to low strength but improved tensile ductility [13]. The lattice distortion of Al matrix was increased by excess Mg element that decreased the conductivity of Al-Mg-Si alloys [14].

Besides the main alloying elements of Mg and Si, some other alloying elements have been found to affect the precipitation in

* Corresponding author.
E-mail address: wangrh@xaut.edu.cn (R. Wang).

https://doi.org/10.1016/j.jmst.2019.03.011
1005-0302/

the Al-Mg-Si alloys. Typically, Cu addition can significantly change the precipitation behavior [15–17], where metastable Q' and stable Q phases with chemical composition of $Al_4Cu_2Mg_8Si_7$ will be produced. It was claimed [18,19] that the peak strength of Al-Mg-Si alloys was increased with the presence of Cu. In addition, a significant increase in ductility with increasing Cu content was also observed [20] in a Si-excess Al-Mg-Si alloys. This was suggested to be due to an improved coherency between the grain boundary precipitates and the aluminum matrix. Besides, Fe or Mn addition will promote the formation of Si-containing primary particles during casting or homogenization treatment [21], which will in turn impact on the following Si-containing precipitation during aging treatment. These indicate that the effect of some other alloying elements is somewhat associated with the change in relative content between the Mg and Si available for precipitation.

Another approach on microstructural design in the Al-Mg-Si alloys was recently proposed by Valiev et al. [22,23], where an intelligent nanostructural design enabled to increase the strength and simultaneously raise the electrical conductivity. This approach was based on a combination of grain refinement down to ultrafine length scale with accelerated formation of nanoprecipitates within the grain interior. The high strength was mainly contributed by grain boundary strengthening, dislocation hardening, and precipitate hardening; and the enhanced electric conductivity was associated with a promoted intragranular precipitation and concomitantly a very low content of solute atoms within the Al matrix. This means that the strength-conductivity inverse correlation could be broken through in the ultrafine grained Al-Mg-Si alloys. However, the effect of Mg/Si ratio on precipitations and hence on strength/conductivity combination have been hardly studied in the ultrafine grained Al-Mg-Si alloys. Grain size dependence of the Mg/Si ration effect is far from clear.

In this work, Al-Mg-Si-Sc alloys with two different Mg/Si ratio (one with Mg excess and the other with Si excess) and with two different grain size (coarse grains vs ultrafine grains) will be studied for comparison to reveal the grain size-dependent Mg/Si ratio effect on microstructural evolution and hardness/electrical conductivity. Since the Al-Mg-Si alloys are widely used as conductors for overhead power line, electrical properties will be also concentrated in this work besides the hardness. The Al-Mg-Si-based conductors used in industrials, usually cold-drawn to wires and finally subjected to artificial aging treatment, generally have grains with size at submicron length scale [24,25]. Since the ultrafine grains are in a high energy condition and are apt to coarsen when exposed to artificial aging, a minor Sc is invariably added in present Al-Mg-Si alloys, which is utilized to form Al_3Sc dispersoids to stabilize the ultrafine grains.

2. Experimental

The Al-Mg-Si-Sc alloys used in present work were melted and cast in a steam argon, by using 99.7 wt% industry pure Al, 99.9% pure Mg, Al-20.0 wt% Si master alloy, and Al-2.0 wt% Sc master alloy. Two alloys with different Mg/Si ratios were studied, *i.e.*, #1 alloy with Mg/Si ratio = 2.38 (Mg excess), and #2 alloy with Mg/Si ratio = 1.10 (Si excess). Composition of the studied Al-Mg-Si-Sc alloys is listed in Table 1. The cast ingots were divided into two parts. The one part was subjected to solid solution treatment at 560 °C for 2 h, followed immediately by artificial aging treatment at 200 °C for a series of times. The alloys undergone these treatments are defined as #1-I and #2-I, respectively. The other part, cut to pieces with the sizes of 20 × 20 × 200 mm, was firstly subjected to solid solution treatment at 560 °C for 2 h, and subsequently extruded to a diameter of 9.5 mm by using the LJ300 extrusion forming machine at an extrusion temperature of ~500 °C. The extruded alloys were finally aged at 200 °C for a series of times. Correspondingly, the alloys with these treatments are defined as #1-II and #2-II, respectively. It is obvious that the difference between the #1-I and #2-I ((or #2-I and #2-II) alloys is that a severe plastic deformation of about 50% reduction is applied in the latter one before aging treatment. All the temperatures are within an error of ± 2 °C. Note that the aging temperature for coarse-grained Al-Mg-Si alloys is generally adopted within 170–190 °C, here in present work the choice of 200 °C as aging temperature is because that the added Sc atoms have a very slow diffusion ability in the Al matrix. To advance the interaction between the Sc atoms and the main alloying elements (Mg and Si), a slightly-elevated aging temperature (*i.e.*, 200 °C) is designed that is expected to promote the Sc diffusion and affect the Mg-Si-based precipitation obviously.

Microstructures of the four alloys were characterized by using an optical microscope (OM) and a transmission electron microscope (TEM). The TEM examinations were performed on a JEOL-2100 microscope operating at 200 kV. The TEM foils were prepared following the standard electro-polishing techniques for Al alloys. Details about the measurements on grain size and precipitate parameters were referred to previous publications [25–27]. Volume fraction of the precipitates was determined by employing a corrected projection method [25], in which the foil thickness of each captured region was obtained through convergent beam electron diffraction patterns [25–27].

Dislocation density was measured by performing X-ray diffraction (XRD) experiments. Each sample was tested at least six times to obtain a set of diffraction profiles. The evaluation of these profiles was done following the Multiple Whole Profile (MWP)-fit method developed by Ungar and co-workers [28,29], where simulated profiles are fitted to the recorded profiles. This is done for all reflections simultaneously with ab initio theoretical functions for the strain- and size-induced profile broadening. The reader can refer to reference [30] for experimental details.

Vickers hardness (HV) was tested on a LECO Hardness Tester (LV700AT) under a weight of 5 kg, with a dwelling time of 10 s. Average HV was determined over at least 9 measurements. Based on samples with gauge size of 1200 mm (standard measurement length of 1000 mm), electrical resistivity was measured by a double direct current electric bridge at room temperature, with the resistivity converted into %IACS (IACS: International Annealed Copper Standard). The following relation was used to express in IACS units: $IACS = \omega_{Al}/\omega_{Cu} \times 100\%$, where ω_{Al} is the conductivity of the studied Al alloy in MS/m and ω_{Cu} is the conductivity of annealed copper (58.0 MS/m).

3. Results and discussion

3.1. Microstructural evolution

Fig. 1 shows representative OM images of the #1-I and #2-I alloys after solid solution treatment and corresponding statistical results on the grain size. Grains in the two alloys are approximately equiaxed, and the average grain size is ~700 μm in the #1-I alloy and ~500 μm in the #2-I alloy. Grains in the I-type alloys were almost unchanged during following artificial aging treatment. Fig. 2(a) and (b) show representative TEM images of the #1-I and #2-I alloys aged at 200 °C for 6 h, respectively, for comparison. Needle-shaped precipitates, determined as β'' phase (see Fig. 2(c) and (d)), are found to disperse within the grain interior in both the two alloys. However, the precipitates in the #2-I alloy have a much more number density (~5.6×10^{21} m^{-3}) and finer size (half needle length ~30 nm) than in the #1-I alloy (number density of ~8.4×10^{21} m^{-3} and half needle length ~46 nm). The difference can be more obviously manifested in Fig. 2(e) and (f), where the average precipitate size and

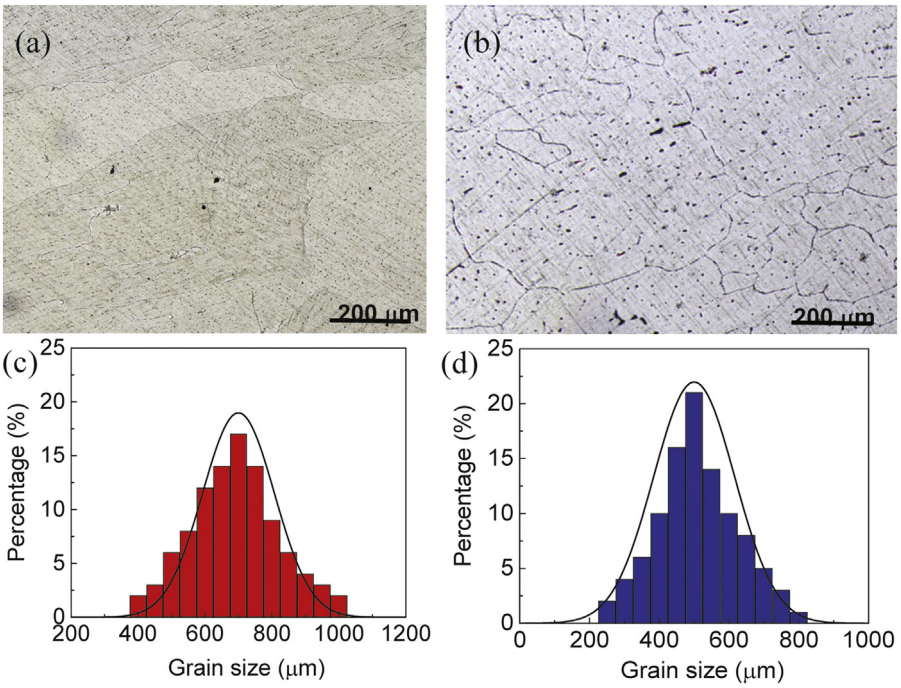

Fig. 1. Representative OM images ((a) and (b)) and corresponding statistical grain size distribution ((c) and (d)) of the #1-I ((a) and (c)) and #2-I ((b) and (d)) alloys, respectively.

precipitate number density are respectively shown as a function of aging time *t*. Previous report [18] have revealed that both excess Mg and excess Si did not alert the precipitation sequence, structure and lattice parameters of the metastable precursors in the Al-Mg-Si alloys. However, excess Si would promote the precipitation of fine, uniformly distributed β'' precipitates. The reason is that excess Si modifies the Mg/Si ratio in the clusters and zones and alters their size, number, density, distribution, stability, and following precipitation [9]. The present experimental results are in good agreement with the previous experimental observations.

In the aged I-type alloys of #1-I and #2-I, no Al_3Sc precipitates were detected. This is reasonable because the aging temperature required for precipitating Al_3Sc nanoparticles is usually above 250 °C, which is greater than present aging temperature of 200 °C. Al_3Sc dispersoids were also hardly found. The absence of Al_3Sc dispersoids is mainly attributed to a high temperature of 560 °C adopted in the solid solution treatment that is enough to dissolve the Al_3Sc dispersoids. The Sc atoms may have some effects on the β'' precipitation. The diffusion coefficient of Si ($\approx 2.1 \times 10^{-4}$ exp (-136 kJ/*RT*) m^2/s) in Al matrix, much greater than the Mg ($\approx 1.2 \times 10^{-5}$ exp (-131 kJ/*RT*) m^2/s), is several orders of magnitude greater than that of the Sc ($\approx 1.9 \times 10^{-4}$ exp (-164 kJ/*RT*) m^2/s) [31]. In the present Al-Mg-Si-Sc alloys, Si-Sc pairs are ready to form thermodynamically due to a high negative enthalpy between the two atoms (~ -207 kJ/mol [32]). This hints that the originally fast Si atoms would be captured and slowed down by the Sc atoms, which will highly inhibit the precipitate growth. In contrast, the Mg atom diffusion is slightly affected by the Sc addition due to their weak Mg-Sc binding (with an enthalpy of only ~ -13 kJ/mol [32]). The Sc-induced decrease in Si solute atom diffusion can thus reduce growth rate of the β'' precipitates. Note that the β'' precipitates were seldom observed in the Al-Mg-Si alloys when aged up to above 190 °C. However, a recent paper reported [33] that some β'' precipitates were still survived after the Al-Mg-Si alloy aged at 230 °C. In present work with aging temperature of 200 °C, the abundant existence of β'' precipitates may be related to the influence of Sc atoms on the Si diffusion that impacts on the progress of precipitation. Comparison between the Al-Mg-Si and Al-Mg-Si-Sc alloys will be presented elsewhere and not discussed in this paper.

Fig. 3 shows representative TEM images of the #1-II and #2-II alloys after extrusion and corresponding statistical results on the cross-sectional grain size. The plastic deformation in extrusion highly refines the grains, causing the cross-sectional grain size at the submicron length scale. The grains with size in submicron in the extruded II-type alloys (average cross-sectional grain size of ~780 nm in the #1-II alloy (Fig. 3(a) and (c)) and ~720 nm in the #2-II alloy (Fig. 3(b) and (d))), usually termed as ultrafine grains, are about three orders of magnitude smaller than the grains of the I-type alloys. Al_3Sc dispersoids with diameter in 30–50 nm are observed in both the two II-type alloys, mainly located at the grain boundaries (as marked by arrows in Fig. 3(b) and (e)). The volume fraction of Al_3Sc dispersoids is about 0.4 vol.% in the #2-II alloy, greater than ~0.1 vol.% in the #1-II one. These dispersoids were created during extrusion that was performed at 500 °C, a temperature at top of the temperature range for forming Al_3Sc particles. All the intergranular dispersoids were conformed to be Al_3Sc particles, and no Mg-Si compounds were detected in the as-extruded II-type alloys. The intergranular Al_3Sc dispersoids are especially effective in hindering the grain growth during hot extrusion, through Zener-drag action [34]. Since the Si-Sc pairs are strong and excess Si can promote the Sc diffusion to grain boundaries, more intergranular Al_3Sc dispersoids were hence created in the #2-II alloy, leading to smaller grain size when compared with the #1-II alloy. Note that there are a few fine Al_3Sc dispersoids in size of about 10 nm distributed within the grain interior of the #2-II alloy, as typically shown in Fig. 3(f).

Previous studies [35–39] clearly showed that the precipitation in ultrafine grained Al alloys was much different from that in traditional Al alloys with coarse grains. The main reason is that there exists a large fraction of grain boundaries in the ultrafine grained alloys and the grain boundary energy is much higher. A typical example is that, in the ultrafine-grained Al-Cu alloy, the precipitation of strengthening metastable θ' particles within the grains

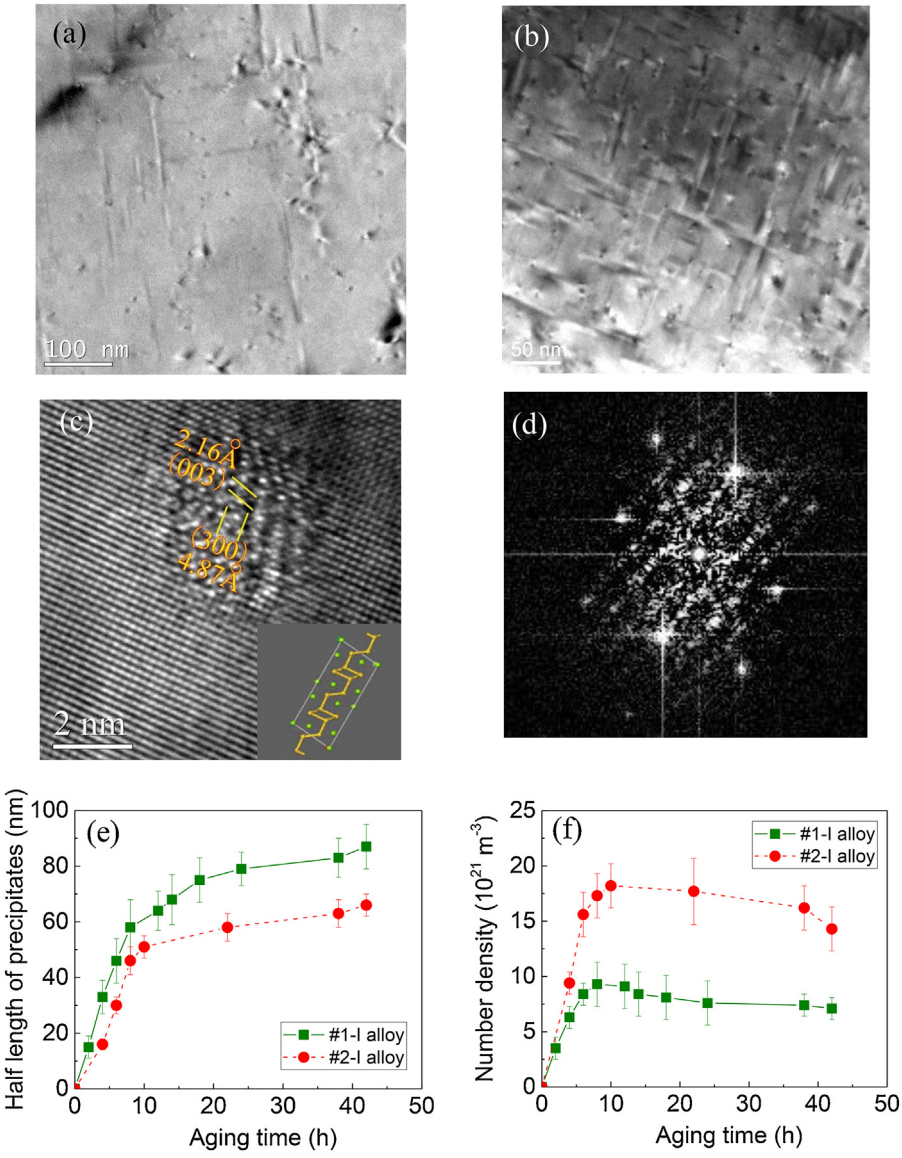

Fig. 2. Representative TEM images showing intragranular β'' precipitates in the #1-I (a) and #2-I (b) alloys aged for 6 h, respectively. (c) and (d) are representative high resolution TEM image and corresponding Fourier Transformation image of a β'' precipitate, respectively. Insert in (c) is a sketch to show the atomic structure of the β'' precipitate along <010> direction. The half needle length and number density of the β'' precipitates are depicted in (e) and (f), respectively, as a function of aging time.

was depressed, while the equilibrium θ-Al_2Cu particles were favorably precipitated at grain boundaries, contrary to what observed in the coarse-grained Al-Cu alloys [35,36,40]. Similarly, Lavernia group's studies [38,39] revealed that grain boundary precipitation dominated in ultrafine-grained Al-Zn-Mg-based alloys. This is because the high volume of grain boundaries led to a low concentration of vacancies in the grain interior, and hence hindered homogeneous nucleation of intragranular precipitates during aging [38,39]. In ultrafine-grained Al-Mg-Si alloys, solute segregation at grain boundaries was also reported by Sauvage et al. [23], which impaired the intragranular precipitation as well. Here in present work, the precipitation in the ultrafine-grained II-type alloys was found to truly deviate from that in their I-type counterparts with coarse grains. Fig. 4 shows representative TEM images of the #1-II and #2-II alloys aged for 6 h, respectively. One can find that (i) in the #1-II alloy with Mg excess, some intragranular needle-shaped β'' precipitates are still found (as typically marked by solid arrows in Fig. 4(c)), like in the coarse-grained #1-I alloy. But both the size (half needle size ~6 nm) and the number density (~3×10^{21} m^{-3}) are remarkably reduced in the #1-II alloy, indicative of a suppressed β'' precipitation in the ultrafine grains. Besides, intragranular Al_3Sc precipitates can be also observed ((as typically marked by open arrows in Fig. 4(c) and also magnified in Fig. 4(e))) that have an average diameter of about 15 nm and a number density of ~8×10^{21} m^{-3}. (ii) in the #2-II alloy, β'' precipitates are no longer existed. Al_3Sc precipitates are also absent. Instead, β' precipitates are sparsely distributed within the grain interior, as shown in Fig. 4(b) and (d). The average size and number density of the β' precipitates are ~8 nm and ~4.2×10^{21} m^{-3}, respectively. (iii) abundant intergranular Mg_2Si particles are found in both the two alloys (typically shown in Fig. 4(f)) and their average size is above ~50 nm. The total volume fraction of intergranular particles, including Mg_2Si particles formed during aging and Al_3Sc dispersoids formed during extrusion, is ~0.3 vol.% in the #1-II alloy and ~0.7 vol.% in the #2-II alloy. Promoted intergranular precipitations are clearly verified in the present ultrafine-grained Al-Mg-Si-Sc alloys, similar to previous reports on ultrafine-grained Al-Cu and Al-Zn-Mg alloys [35,36,38,39]. In particular, more intergranular Mg_2Si particles were produced in the #2-II alloy than in the #1-II alloy.

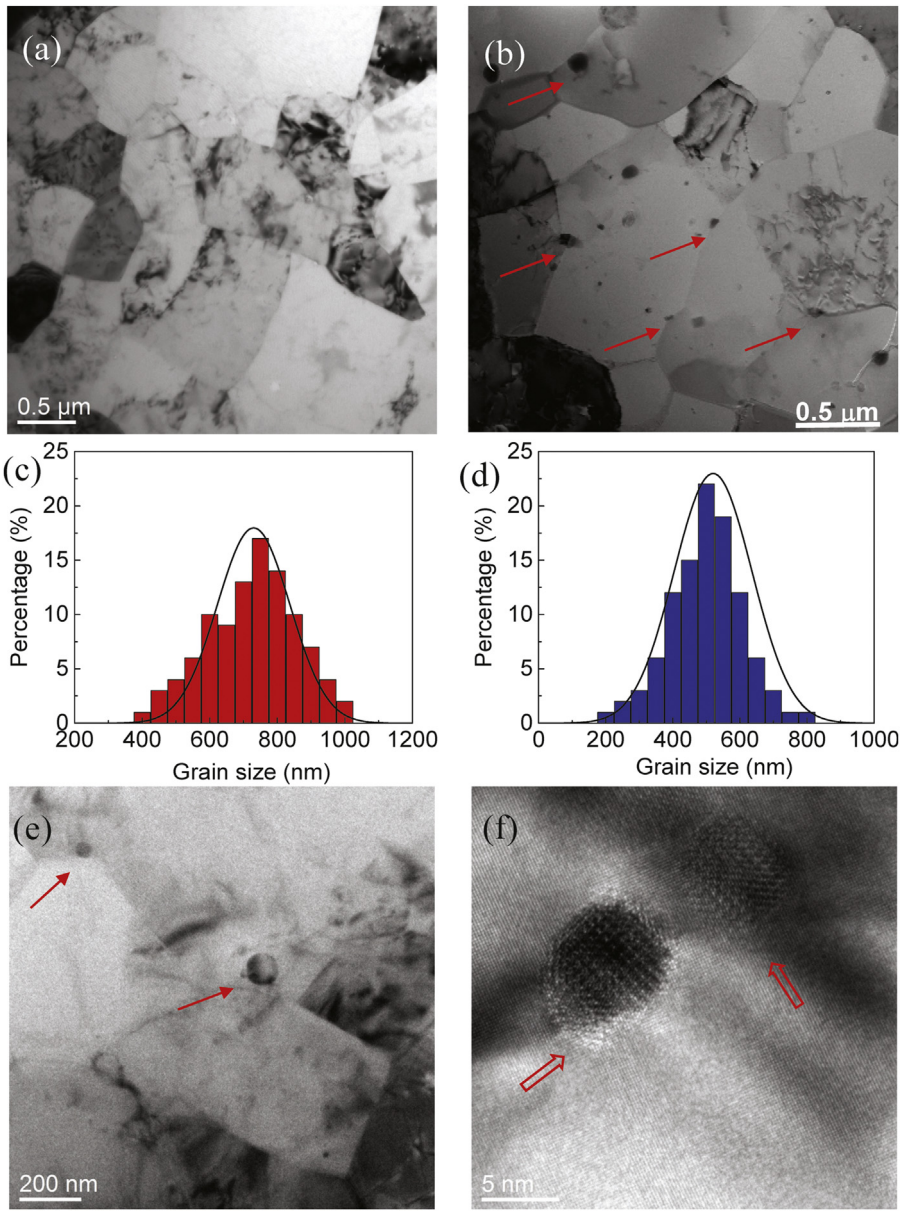

Fig. 3. Representative TEM images ((a) and (b)) and corresponding statistical cross-sectional grain size distribution ((c) and (d)) of the as-extruded #1-II ((a) and (c)) and #2-II ((b) and (d)) alloys, respectively. (e) is a typical TEM image showing some Al3Sc dispersoids located at grain boundaries in the as-extruded #1-II alloy (marked by solid arrows), and (f) showing some fine intragranular Al3Sc dispersoids in the #2-II alloy (marked by open arrows).

At a relative low aging temperature of 200 °C, it is generally believed that the nanosized Al_3Sc precipitates are hardly produced in the coarse-grained Al alloys. In the present ultrafine-grained #1-II alloy aged at 200 °C, however, precipitation of Al_3Sc nanoparticles within the grain interior is clearly found. This is mainly related to the unique microstructure of the ultrafine-grained structure. The high energy stored in the deformed microstructures and much increased defects (e.g., dislocations and vacancies) in the ultrafine grains will highly accelerate the Sc diffusion and promote the driving force for Al_3Sc precipitation. While in the #2-II alloy, Al_3Sc precipitates are hardly found. The main reasons are associated with the Si excess and Si-Sc strong binding. During extruded at a high temperature, the faster Si atoms are ready to diffuse to grain boundaries to reduce the system energy. Due to the strong Si-Sc binding, the Sc diffusion will be sped up and also move forward to the grain boundaries. This is responsible for the experimental finding that the intergranular Al_3Sc dispersoids in the #2-II alloy are much more than in the #1-II one. Since a large part of Sc atoms had been consumed for producing Al_3Sc dispersoids, the available Sc atoms for nanosized Al_3Sc precipitation were highly limited. As a result, the intragranular Al_3Sc precipitates are absent in the #2-II alloy. Instead, the sored high energy and abundant defects in the #2-II alloy turned to promote the β' precipitation by suppressing the β'' phases.

The experimental results on microstructural evolution manifest that the precipitation behaviors in the Al-Mg-Si-Sc alloys are highly dependent on the Mg/Si ratio and the grain size, as schematically illustrated in Fig. 5. The microstructural evolution will impact on the mechanical properties and electrical properties, as discussed below.

3.2. Hardness evolution and strengthening mechanisms

Fig. 6(a) and (b) shows the measured hardness of the I-type and II-type alloys, respectively, as a function of aging time. In the coarse-grained I-type alloys, it is generally found that the hardness

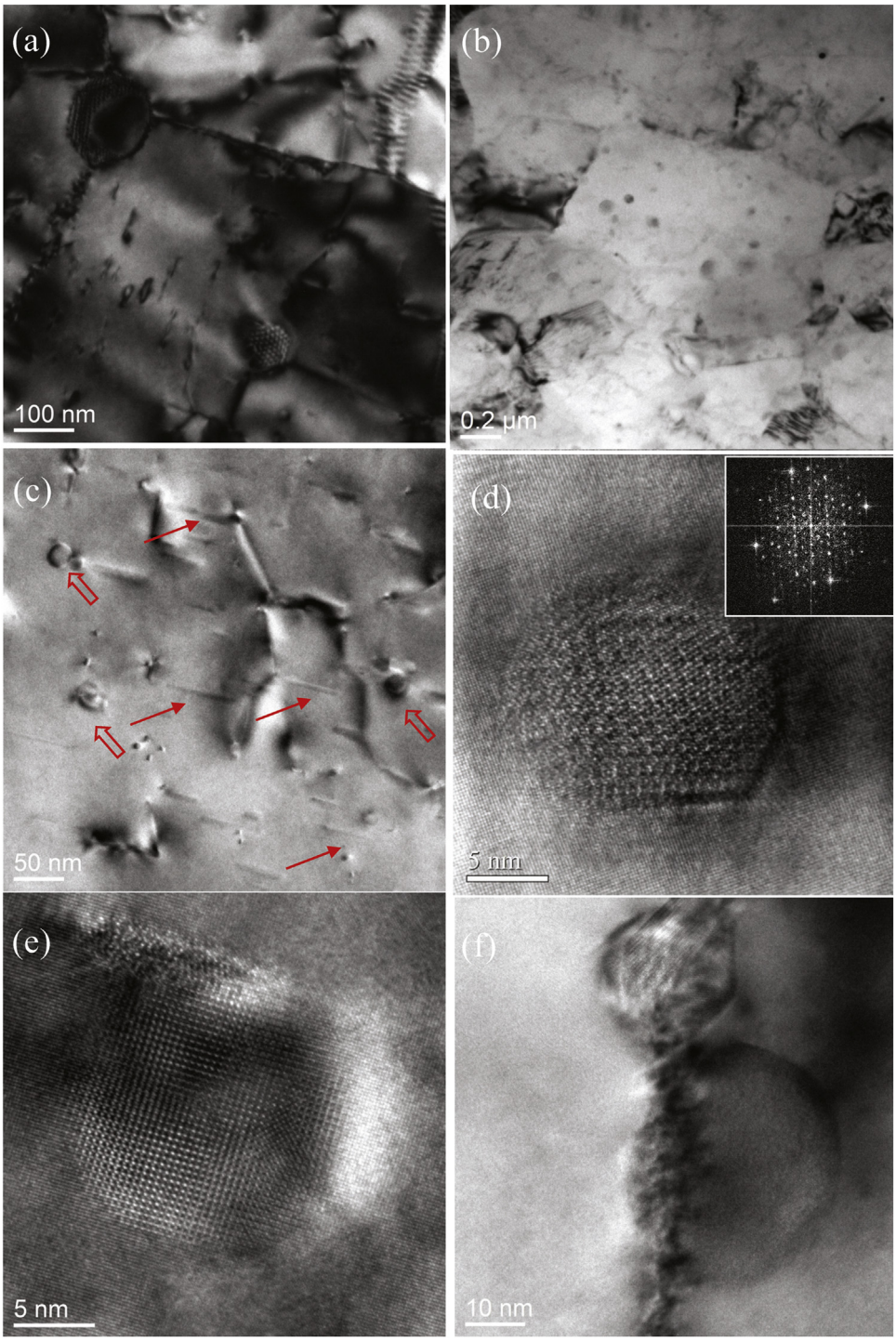

Fig. 4. Representative TEM images showing precipitates in the #1-II ((a), (c), and (e)) and #2-II ((b), (d), and (f)) alloys aged for 6 h, respectively. (a) and (b) are in low magnification, while (c) and (d) in high magnification. The β'' precipitates and Al3Sc precipitates in the aged #1-II alloy are marked by solid and open arrows, respectively, as shown in (c). A β' precipitate in the aged #2-II alloy is typically shown in (d), with corresponding selected-area diffraction pattern inserted in the upper-right corner. (e) shows a representative TEM image of an Al3Sc precipitate in the aged #1-II alloy, and (f) shows a representative TEM image of two Mg2Si particles formed at grain boundary in the aged #2-II alloy.

increases with aging time up to 6–10 hours, thereafter the hardness tends to saturate. The #2-I alloy with Si excess displays hardness much greater than the #1-I alloy with Mg excess, see Fig. 6(a). This is consistent with the microstructure finding that the former alloy contains intragranular β''-Mg_2Si precipitates more than the latter one.

In the ultrafine-grained II-type alloys, however, the hardness decreases rather than increases with aging time (see Fig. 6(b)), contrary to the trend in the coarse-grained I-type alloys. Of special interest to note is that the #1-II alloy with Mg excess is harder than the #2-II alloy with Si excess, opposite to what observed in the I-type alloys. The hardness of #1-II alloy only slightly decreases with increasing aging time, while the #2-II alloy shows time-dependent hardness obviously reduced. The dropping in hardness is mostly attributed to dislocation annihilation and grain growth, as generally found in the ultrafine-grained alloys when subjected to anneal-

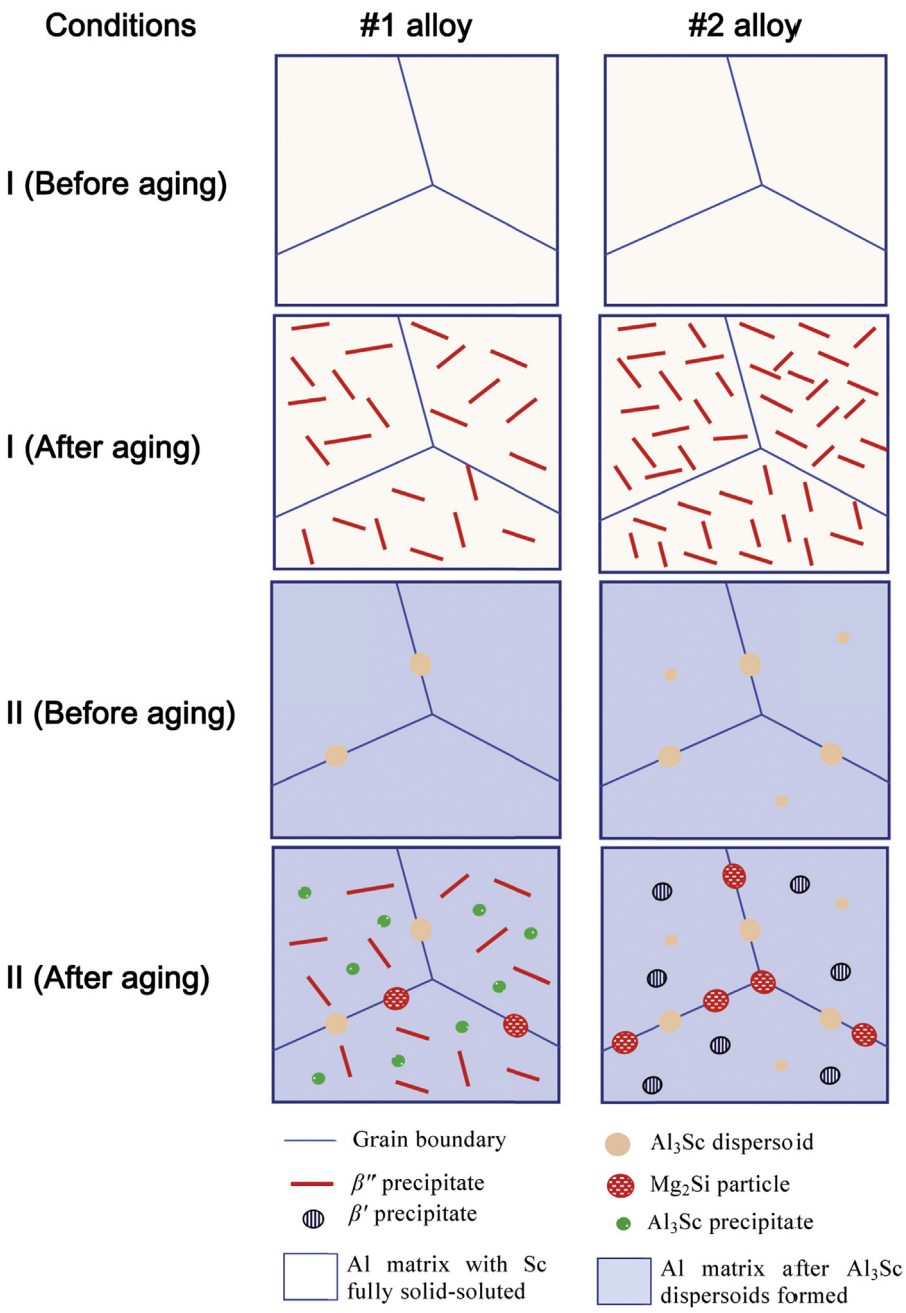

Fig. 5. Sketches to illustrate the microstructural evolution in the coarse-grained and ultrafine-grained #1 and #2 alloys before and after aging treatment.

ing/aging. In the present ultrafine-grained #2-II alloy, the grains underwent inapparent growth during aging treatment due to the grain boundary pinned by Al_3Sc dispersoids. Quantitatively, the statistical results show the grain size increased from about 720 nm before aging to about 850 nm after aged for 6 h. Correspondingly, the dislocation density reduced from about 3.2×10^{14} m^{-2} before aging to about 2.1×10^{14} m^{-2} after aged for 6 h, as measured experimentally. These are responsible for the strength degradation in the #2-II alloy when subjected to artificial aging.

It should be especially mentioned that the #1-II alloy displayed evolution in grain growth and dislocation annihilation close to the #2-II alloy. However, the hardness of #1-II alloy was almost unchanged with aging time, unlike an obvious reduction in the #2-II alloy. This discrepancy is mostly related to the strengthening nanoparticles that are different between in the #1-II alloy and in the #2-II alloy. Refer to the microstructural results presented in above section, the intragranular precipitates in the #1-II alloy are β'' and Al_3Sc, while in the #2-II alloy are only β'. The total volume fraction of precipitates in the former alloy (*e.g.*, ~0.25 vol.% at aged for 6 h) is greater than in the latter one (*e.g.*, ~0.16 vol.% at aged for 6 h). It is well known that the β'' precipitates strengthen the Al-Mg-Si alloys more than the β' precipitates. In addition, the Al_3Sc precipitates have an average size of about 15 nm, which is below the critical size of about 20 nm [41] for losing coherency. This means that the Al_3Sc precipitates in present #1-II alloy are coherent or semi-coherent with the matrix and hence have a notable strengthening response. The strengthening of β'' and Al_3Sc precipitates compensated the decrease in hardness induced by dislocation annihilation and grain growth, keeping the hardness of #1-II alloy stable during aging. While in the #2-II alloy, the softening by dislocation annihilation and grain growth predominated over the β' strengthening, causing the hardness obviously reduced with aging time.

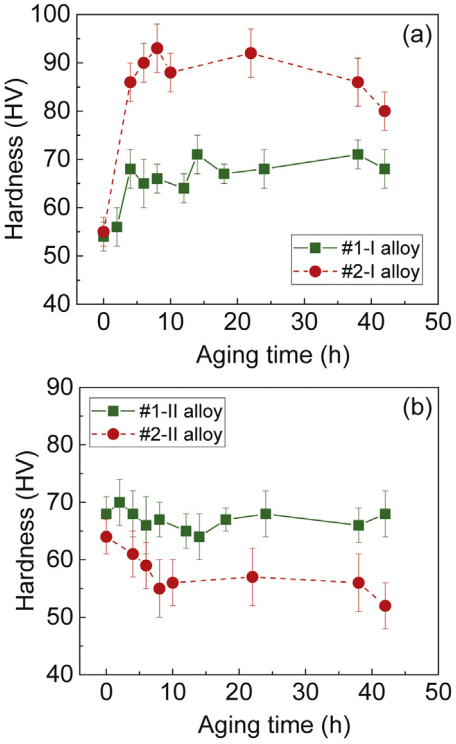

Fig. 6. Hardness evolution in the coarse-grained (a) and ultrafine-grained (b) #1 and #2 alloys as a function of aging time.

Next, we will present a strengthening model to quantitatively describe the hardness of aged I-type alloys that contain only β'' precipitates. The hardness of II-type alloys is not calculated here because the coexistence of intergranular and intragranular particles makes the modeling complicated. Besides, both β'' and Al_3Sc precipitates are simultaneously distributed in the grain interior of the #1-II alloy, and their strengthening effects are also difficult to couple.

The hardness/strength of present coarse-grained Al-Mg-Si-Sc alloys is contributed mainly by the solute atoms, forest dislocations, grain boundaries, and precipitates. Correspondingly, the hardness (H) can be expressed as [42]:

$$H = H_0 + H_{ss} + H_d + H_{gb} + H_p, \quad (1)$$

where H_0 is the base hardness of the pure Al that is arisen from friction stress (taken as 10 HV [27]), H_{ss}, H_d, H_{gb}, and H_p are the contributions by solid solution hardening, forest dislocation hardening, grain boundary strengthening, and precipitate hardening, respectively. The strength related to solid solution hardening (σ_{ss}) is evaluated by [27]:

$$\sigma_{ss} = \sum_i k_i c_i^{2/3}, \quad (i = \text{Mg, Si, and Sc}), \quad (2)$$

where c_i is the concentration of i solute (in wt.%) and k_i is a scaling factor for the i solute: $k_{Mg} \approx 29.0$ MPa (wt.%)$^{-2/3}$, $k_{Si} \approx 66.3$ Mpa (wt.%)$^{-2/3}$, and $k_{Sc} \approx 82.5$ Mpa (wt.%)$^{-2/3}$ [43,44]. The strength associated with the forest dislocation hardening (σ_d) is given by [45]:

$$\sigma_d = M\alpha Gb\sqrt{\rho} \quad (3)$$

where M is the Taylor factor (≈3.0 [45]), α is a constant with a value of approximately 0.14, ρ is the dislocation density that is determined to be about 2×10^{12} m^{-2}, G and b are the shear modulus (28 GPa [46]) and Burgers vector (0.286 nm [46]) of Al, respectively. The strength induced by grain boundary hardening (σ_{gb}) follows the well-known Hall-Petch relationship:

$$\sigma_{gb} = k_{HP} d^{-1/2} \quad (4)$$

with k_{HP} is a scaling constant that is taken as 0.042 MPa/m$^{-1/2}$ for calculation and d is the grain size. The β'' precipitate hardening is expressed by [47]

$$\sigma_p = 2M\beta Gb/\lambda, \quad (5)$$

where β is a constant (≈ 0.28 [47]), M, G and b have been defined above and λ is the mean inter-precipitate spacing that can be estimated by $\lambda = 1/N^{1/3}$ (N is the number density of the precipitates).

It is generally considered that the strength is about three times of the hardness HV [48]. This means that $H_i \approx \sigma_i/3$, with i = *ss*, *d*, *gb*, or *p*. The hardness can then be respectively calculated by using Eq. (1) together with Eqs. (2)–(5), based on the experimental measurements on the grain size, dislocation density, precipitate parameters, *etc*. The calculations on hardness are plotted in Fig. 7 to compare with some experimental results of the aged I-type alloys. It is evident that the calculations are in broad agreement with the experimental data, indicative of the good application of the strengthening model to the coarse-grained Al-Mg-Si-Sc alloys.

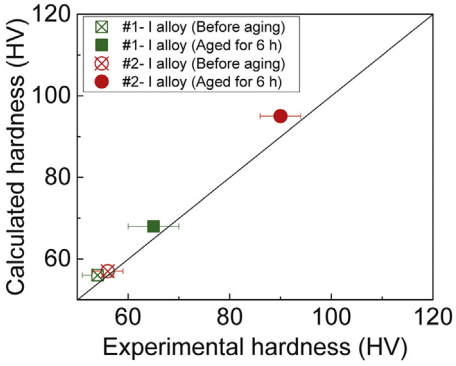

Fig. 7. Calculated hardness in comparison with corresponding experimental data. Note that only the coarse-grained alloys are selected for calculations, and four data (both #1 and #2 alloys: before aging and aged for 6 h) are used for comparison.

3.3. Conductivity evolution and influencing factors

Fig. 8(a) and (b) shows the evolution of electrical conductivity with aging time in the aged I-type and II-type alloys, respectively. It is generally believed [7] that precipitation will increase the electrical conductivity of Al alloys because the detrimental effect of precipitates on electrical conductivity is inferior to that of the solid solutes. Electrical conductivity improved with aging time is truly observed in present Al-Mg-Si-Sc alloys, either in the coarse-grained I-type or in the ultrafine-grained II-type. However, the increase in electrical conductivity with aging time is very slow in the I-type alloys, and the #2-I alloy displays electrical conductivity close to the #1-I alloy although much more β'' are precipitated in the former. The most possible reason is that the precipitates, once in a dense distribution, will impair the electrical conductivity apparently. Raeisinia et al. [7] claimed that, for precipitate spacings on the order of 10 nm, the precipitates accounted for 15%–25% of the total resistivity while this contribution decreased to 10%–15% for spacings in 10–100 nm range. This indicates that the precipitates remarkably affect the electrical conductivity when the inter-precipitate spacing is about several tens nanometers. The inter-precipitate spacing in the #2-I alloy aged for 6 h is estimated to be ≈20 nm, which is much smaller than in the #1-I alloy under the same aging (>50 nm). The negative effect of precipitates on the electrical conductivity competes with the positive effect of reduced

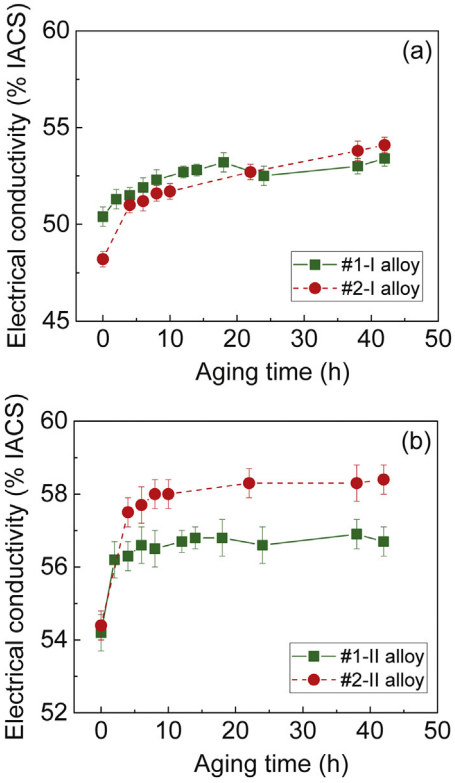

Fig. 8. Electrical conductivity evolution in the coarse-grained (a) and ultrafine-grained (b) #1 and #2 alloys as a function of aging time.

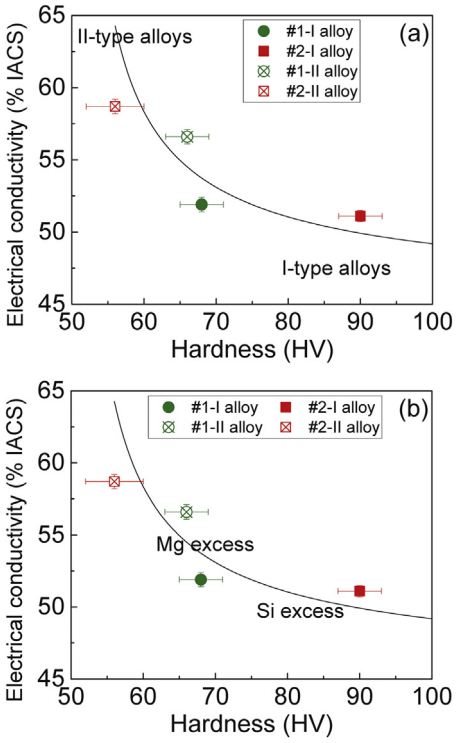

Fig. 9. Hardness-electrical conductivity correlation of present Al-Mg-Si-Sc alloys with different grain size and Mg/Si ratio. The four data are selected from the best hardness/electrical conductivity combination among the four sets of alloys, *i.e.*, aged #1-I, #2-I, #1-II, and #2-II alloys. Two regimes in (a) demonstrate the effect of grain size (I-type vs II-type), while those in (b) manifest the effect of Mg/Si ratio (#1 vs #2). The line is a guide for the eyes.

solid solution atoms, causing the electrical conductivity changed slightly between the two I-type alloys.

The dislocation annihilation and grain growth during aging can also contribute to the increase in the electrical conductivity of the ultrafine-grained II-type alloys. However, these are not the controlling factors. Microstructural examinations showed that the difference in aging-induced dislocation density change and grain coarsening is inapparent between the #1-II and #2-II alloys, while the electrical conductivity is much different (see Fig. 8(b)). The underlying mechanism is then proposed to the Mg_2Si particle formation at the grain boundaries that is highly dependent on the Si promotion, *i.e.*, more intergranular Mg_2Si formed in the #2-II alloy with Si excess than in the #1-II alloy with Mg excess.

According to Mattiessen's rule, the total resistivity of the aged Al-Mg-Si-Sc alloys can be expressed by [24]

$$\rho_{total} = \rho_0 + \rho_{ss} + \rho_d + \rho_{gb} + \rho_p, \quad (6)$$

where ρ_{total} is the total electrical resistance of the alloy, ρ_0 is the intrinsic electrical resistivity of the lattice, ρ_{ss} is the resistivity due to the Mg, Si, and Sc solute atoms dissolved in the Al matrix ($\rho_{ss} = \sum_i \rho_i c_i$, $i =$ Mg, Si, and Sc,), ρ_d is the resistivity due to the dislocations, ρ_{gb} is the resistivity due to grain boundaries, and ρ_p is the resistivity induced by intragranular precipitates. Although the total electrical resistance or electrical conductivity is affected by many factors, a conclusion can be drawn from above discussions that the factor playing a decisive role is the solute atoms dissolved in the Al matrix. In the case of more Mg_2Si particles formed at the grain boundaries such as in the #2-II alloy, the solute atoms in the matrix will be greatly reduced, which results in a significant improvement in the electrical conductivity.

3.4. Hardness-conductivity relationship

In metals including the Al alloys, it is generally found [8] that the strength/hardness and electrical conductivity are mutually exclusive. This means that all the approaches to increase strength/hardness unexceptionally lead to a pronounced decrease in conductivity. An inverse hardness-conductivity correlation can be similarly observed in present Al-Mg-Si-Sc alloys, as shown in Fig. 9 where some representative data (best hardness/electrical conductivity combination) from different Mg/Si ratio and grain size are depicted. One can see from Fig. 9(a) that the I-type alloys are apt to have a high hardness while the II-type alloys to have a high electrical conductivity. While from Fig. 9(b), it is clear that both the hardness and the electrical conductivity can be tailored within a wide range in the Al-Mg-Si-Sc alloys with Si excess. In the Al-Mg-Si-Sc alloys with Mg excess, however, neither the hardness nor the electrical conductivity could be greatly regulated even manipulating the grain size from micro to submicron length scale.

The hardness-conductivity inverse correlation is still unsatisfactorily held in present Al-Mg-Si-Sc alloys. The coarse-grained alloys (precipitates mainly distributed within the grain interior) generally have high hardness but low electrical conductivity. While the ultrafine-grained alloys (with a majority of particles located at grain boundaries) show enhanced electrical conductivity by sacrificing hardness. Valiev et al. [22,23] realized a simultaneous improvement in hardness/strength and electrical conductivity by refining grains down to ultrafine length scale and accelerating formation of nanoprecipitates within the grain interior. The key in preparing technology they utilized is dynamic aging during severe plastic deformation processing, *i.e.*, the grain refinement and nanoparticle precipitation happened concurrently. While in our work, the aging treatment was carried out following severe

plastic deformation, which caused adverse intergranular precipitations. In further work, dynamic aging instead of post aging should be adopted for the Al-Mg-Si-based alloys that may result in superior strength/conductivity combination. This attempt is now being undertaken for our Al-Mg-Si-Sc alloys in particular with the Si excess.

4. Conclusions

(1) The coarse-grained Al-Mg-Si-Sc alloy with Si excess exhibited age hardening much greater than that with Mg excess. This is related to the significant Si-promoted β'' precipitation within the grain interior. The electrical conductivity, however, was relatively insensitive to the Mg/Si ratio. The reason is that the dense precipitates with spacing of several tens nanometers impair the electrical conductivity remarkably, which is comparable to the detrimental effect of solute atoms.

(2) The ultrafine-grained Al-Mg-Si-Sc alloy with Si excess displayed highly enhanced electrical conductivity after aging, which was much greater than the alloy with Mg excess. More Mg_2Si particles formed at grain boundaries in the former alloy is responsible for this discrepancy. The alloy with Si excess showed apparent aging softening, while the alloy with Mg excess held the hardness almost changed during aging. These can be rationalized by considering the difference in microstructure: β'' precipitates and some Al_3Sc precipitates were created within the grain interior in the alloy with Mg excess, while only less-strengthening intragranular β' precipitates in low volume fraction were produced in the alloy with Si excess.

(3) The grain size-dependence of Mg/Si ratio effect on the precipitation and mechanical/electrical properties is summarized for present Al-Mg-Si-Sc alloys. Both the hardness and electrical conductivity can be tailored in a wide range in the case of Si excess, while the window is significantly shrunk in the case of Mg excess.

Acknowledgement

This work is financially supported by the National Natural Science Foundation of China (No. 51771147).

References

[1] S. Esmaeili, X. Wang, D.J. Lloyd, W. Poole, Metall. Mater. Trans. A 34 (2003) 751–763.
[2] M.A. van Huis, J.H. Chen, M.H.F. Sluiter, H.W. Zandbergen, Acta Mater. 55 (2007) 2183–2199.
[3] K. Yoshida, K. Doi, Procedia Eng. 81 (2014) 706–711.
[4] S. Karabay, Mater. Des. 27 (2006) 821–832.
[5] A. Serizawa, T. Sato, M.K. Miller, Mater. Sci. Eng. A 561 (2013) 492–497.
[6] M. Liu, J. Čížek, C.S.T. Chang, J. Banhart, Acta Mater. 91 (2015) 355–364.
[7] B. Raeisinia, W.J. Poole, D.J. Lloyd, Mater. Sci. Eng. A 420 (2006) 245–249.
[8] M.Y. Murashkin, I. Sabirov, X. Sauvage, R.Z. Valiev, J. Mater. Sci. 51 (2016) 33–49.
[9] A.K. Gupta, D.J. Lloyd, S.A. Court, Mater. Sci. Eng. A 316 (2011) 11–17.
[10] H. Zhong, P.A. Rometsch, Y. Estrin, Metall. Mater. Trans. A 44 (2013) 3970–3983.
[11] L.P. Ding, Z.H. Jia, Z.Q. Zhang, R.E. Sanders, Q. Liu, G. Yang, Mater. Sci. Eng. A 627 (2015) 119–126.
[12] H. Zhong, P.A. Rometsch, L.F. Cao, Y. Estrin, Mater. Sci. Eng. A 651 (2016) 688–697.
[13] A.K. Sachdev, Metall. Mater. Trans. A 21 (1990) 165–175.
[14] X.X. Xu, Z. Yang, Y.L. He, G.X. Wang, X.L. He, Mater. Charact. 119 (2016) 114–119.
[15] D.J. Chakrabarti, D.E. Laughlin, Prog. Mater. Sci. 49 (2004) 389–410.
[16] C.D. Marioara, S.J. Andersen, T.N. Stene, H. Hasting, J. Walmsley, A.T.J. Van Helvoort, R. Holmestad, Philos. Mag. 87 (2007) 3385–3413.
[17] K. Matsuda, Y. Uetani, T. Sato, S. Ikeno, Metall. Mater. Trans. A 32 (2001) 1293–1299.
[18] M.S. Remøea, K. Marthinsen, I. Westermann, K. Pedersen, J. Røyset, C. Marioara, Mater. Sci. Eng. A 693 (2017) 60–72.
[19] D.J. Chakrabarti, Y. Peng, D.E. Laughlin, Mater. Sci. Forum 396–402 (2002) 857–862.
[20] Y. Kato, K. Hisayuki, M. Sakaguchi, K. Higashi, Proceedings of the 13th International Conference on Aluminum Alloys, 2012, pp. 1521–1526.
[21] Q.R. Zhao, Z. Qian, X.L. Cui, Y.Y. Wu, X.F. Liu, J. Alloy Compd. 666 (2016) 50–57.
[22] R.Z. Valiev, M.Y. Murashkin, I. Sabirov, Scripta Mater 76 (2014) 13–16.
[23] X. Sauvage, E.V. Bobruk, M.Y. Murashkin, Y. Nasedkina, N.A. Enikeev, R.Z. Valiev, Acta Mater. 98 (2015) 355–366.
[24] Y. Han, D. Shao, B.A. Chen, Z. Peng, Z.X. Zhu, Q. Zhang, X. Chen, G. Liu, X.M. Li, J. Mater. Sci. 52 (2017) 4445–4459.
[25] S.Y. Jiang, R.H. Wang, Sci. Reports 8 (2018) 6202.
[26] S.P. Yuan, G. Liu, R.H. Wang, G.J. Zhang, X. Pu, J. Sun, K.H. Chen, Scripta Mater. 60 (2009) 1109–1112.
[27] S.P. Yuan, G. Liu, R.H. Wang, X. Pu, G.J. Zhang, J. Sun, K.H. Chen, Scripta Mater. 57 (2007) 865–868.
[28] T. Ungár, J. Gubicza, G. Ribárik, A. Borbély, J. Appl. Crystallogr. 34 (2001) 298–310.
[29] J. Gubicza, L. Balogh, R.J. Hellmig, Y. Estrin, T. Ungár, Mater. Sci. Eng. A 400 (2005) 334–338.
[30] J. May, M. Dinkel, D. Amberger, H.W. Höppel, M. Göken, Metall. Mater. Trans. A 38 (2007) 1941–1945.
[31] L.F. Mondolfo, Aluminum Alloys: Structure and Properties, Butterworths, 1976.
[32] A.K. Niessen, F.R. de Boer, R. Boom, P.F. de Chatel, W.C.M. Matterns, ALPHAD 7 (1983) 51–70.
[33] G.Y. Lin, Z.P. Zhang, H.Y. Wang, K. Zhou, Y.Y. Wei, Mater. Sci. Eng. A 650 (2016) 210–217.
[34] M. Ferry, N.E. Hamilton, F.J. Humphreys, Acta Mater. 53 (2005) 1097–1109.
[35] L. Jiang, J.K. Li, G. Liu, R.H. Wang, B.A. Chen, J.Y. Zhang, J. Sun, M.X. Yang, G. Yang, J. Yang, X.Z. Cao, Mater. Sci. Eng. A 637 (2015) 139–154.
[36] Y. Huang, J.D. Robson, P.B. Prangnell, Acta Mater. 58 (2010) 1643–1657.
[37] W. Chrominski, M. Lewandowska, Acta Mater. 103 (2016) 547–557.
[38] T. Hu, K. Ma, T.D. Topping, J.M. Schoenung, E.J. Lavernia, Acta Mater. 61 (2013) 2163–2178.
[39] K. Ma, T. Hu, H. Yang, T.D. Topping, A. Yousefiani, E.J. Lavernia, J.M. Schoenung, Acta Mater. 103 (2016) 153–164.
[40] B.A. Chen, G. Liu, R.H. Wang, J.Y. Zhang, L. Jiang, J.J. Song, J. Sun, Acta Mater. 61 (2013) 1676–1690.
[41] S. Iwamura, Y. Miura, Acta Mater. 52 (2004) 591–600.
[42] Y. Chen, N. Gao, G. Sha, S.P. Ringer, M.J. Starink, Acta Mater. 109 (2016) 202–212.
[43] J. Røyset, N. Ryum, Int. Mater. Rev. 50 (2005) 19–44.
[44] O.R. Myhr, Ø. Grong, S.J. Andersen, Acta Mater. 49 (2001) 65–75.
[45] J.E. Bailey, P.B. Hirsch, Philos. Mag. 5 (1960) 485–497.
[46] G. Liu, G.J. Zhang, X.D. Ding, J. Sun, K.H. Chen, Mater. Sci. Eng. A 344 (2003) 113–124.
[47] D. Bardel, M. Perez, D. Nelias, A. Deschamps, C.R. Hutchinson, D. Maisonnette, T. Chaise, J. Garnier, F. Bourlier, Acta Mater. 62 (2014) 129–140.
[48] A. Deschamps, F. Livet, Y. Bréchet, Acta Mater. 47 (1998) 281–292.